Lab on a Chip

PAPER

View Article Online
View Journal | View Issue

Cite this: *Lab Chip*, 2025, **25**, 6533

Application of a bioengineered intestinal epithelium for drug permeability and metabolism studies

Elisabeth Gill,†[ab] Stephanie Muenchau Schoepp, †[ag] Sina Simon,[b] Marius F. Harter,[ac] Mikhail Nikolaev,[a] Iago Pereiro, [a] Inês Silva,[a] Rubén López-Sandoval, [ad] Marco Berrera, [e] Tony Kam-Thong,[e] Marco Michalski,[f] Michael Zaayman,[f] Julien Aubert,[a] Irineja Cubela,[a] Janneke Keemink,[b] Cordula Stillhart,[g] Michael Hofmann, [g] Stephen Fowler, [b] J. Gray Camp,[ah] Nicolo Milani‡*[b] and Nikolche Gjorevski ‡*[a]

The small intestine is the most important site of absorption for many orally administered drugs. Following absorption, intestinal and hepatic first-pass metabolism reduce the amount of drug that reaches the systemic circulation and hence the intended therapeutic target. *In vitro* models can be used to predict intestinal permeability and metabolism, enabling optimization of drug candidate properties for improved oral bioavailability. Currently, data from separate metabolism and permeability assays is combined using modelling approaches, but this does not allow for assessment of interconnected processes. An *in vitro* system which captures both intestinal permeability and metabolism could improve human pharmacokinetics (PK) prediction accuracy. In this study, a human organoid based bioengineered intestinal epithelium (BIE) with apical and basolateral partitioning and crypt-axis patterning was characterized with regards to barrier function as well as the presence of key drug-metabolizing enzymes (DMEs) and drug transporters (DTs). Drug transport studies validated the function of P-glycoprotein (P-gp) and breast cancer resistance protein (BCRP) through targeted inhibition. Furthermore, the BIE's capability to estimate drug metabolic parameters is demonstrated through mathematical mechanistic modeling to predict the fraction escaping gut metabolism (F_g). Results indicate consistent tissue patterning and the potential to assess drug permeability and metabolism in the gut simultaneously. The use of intestinal organoids in a microphysiological system coupled with *in silico* modeling holds significant promise to innovate oral drug bioavailability assessment and aid in drug formulation and safety screening.

Received 24th June 2025,
Accepted 15th September 2025

DOI: 10.1039/d5lc00626k

rsc.li/loc

Introduction

Understanding intestinal drug permeability and metabolism is essential for successful design and development of novel orally administered therapeutics. Oral bioavailability, which is defined as the fraction of an orally taken drug that reaches systemic circulation, is a product of the fraction of drug absorbed (F_a, primarily in the intestine), as well as the fraction that escapes both gut (F_g) and liver metabolism (F_h).[1] When researching new drugs for potential clinical application, not only their solubility, efficacy and toxicity needs to be evaluated, but also how well the compound permeates across the intestinal barrier. The ability to diffuse passively across biological membranes is one of the most critical of the properties evaluated early in drug discovery to inform about the usability of a compound as an orally delivered drug, especially if the compound must subsequently diffuse through target tissue barriers. Additionally, the influence of drug transporters (DTs) and drug metabolizing enzymes (DMEs) on drug permeation is a crucial factor to be investigated, since they play a major role in drug disposition and drug–drug interactions (DDIs).[2] Standard *in vitro* systems

[a] *Institute of Human Biology (IHB), Roche Pharma Research and Early Development, Roche Innovation Center Basel, Basel, Switzerland. E-mail: nikolche.gjorevski@roche.com*
[b] *Pharmaceutical Sciences, Roche Innovation Center Basel, Roche Pharma Research and Early Development, Basel, Switzerland. E-mail: nicolo.milani@roche.com*
[c] *Gustave Roussy Cancer Campus, University Paris-Saclay, Paris, France*
[d] *Department of Biosystems Science and Engineering, ETH Zürich, Basel, Switzerland*
[e] *Data & Analytics, Roche Pharma Research and Early Development, Roche Innovation Center Basel, Basel, Switzerland*
[f] *360 Labs, Strategy, Portfolio and Operations (SPO), Roche Pharma Research and Early Development, Roche Innovation Center Basel, Basel, Switzerland*
[g] *Roche Pharmaceutical Research and Development, Synthetic Molecules Technical Development, Basel, Switzerland*
[h] *Biozentrum, University of Basel, Basel, Switzerland*
† Co-first authors.
‡ Co-corresponding authors.

either lack adequate expression of intestinal DTs and DMEs or inherently have no barrier function and cannot be cultured for extended times. For example, cell-free barrier models such as parallel artificial membrane permeability assay (PAMPA) or cell lines such as Caco-2 on transwell (TW) offer a robust and high-throughput model of compound permeation. PAMPA assays are used to assess passive transcellular permeability in high throughput, whereas cell lines overexpressing efflux transporters such as P-glycoprotein (P-gp) and breast cancer-resistant protein (BCRP) are applied to capture reverse transport into the intestinal lumen. These systems either have no metabolic function, including cytochrome P450 3A4 (CYP3A4)-mediated activity, or, in the case of Caco-2, may not accurately reflect metabolic activity within the small intestine.[3] Microsomes, suspended enterocytes, and cryopreserved intestinal fragments are therefore used in a separate assay to predict intestinal clearance through measuring compound depletion and metabolite formation. Owing to their limited lifespan of several hours, these systems do not capture metabolic dynamics fully,[4] and are unsuitable for drug transport studies. Since membrane permeability, residence time in the cells, and metabolic activity are closely interconnected and affect F_g, there is a strong need for a more physiologically representative system where both can be assessed and predicted simultaneously.

Human intestinal organoids, generated from biopsies of the small intestine and colon, offer greater physiological mimicry of cell diversity and tissue architecture, with presence of the characteristic drug metabolizing enzymes and transporters.[5–7] Aside from applications in stem cell biology, organ development, function and disease, organoids are increasingly utilized in pharmaceutical studies, including those related to drug metabolism and permeation. For example, organoids have been used to characterize intestinal region-specific expression of transport- and absorption-related genes, drug permeability and efflux ratios.[8,9] To circumvent the issue of luminal inaccessibility within conventional organoids cultured in domes, researchers have investigated intestinal transport using static TW monolayers[8] and perfused organ-on-chip systems.[10,11] Indeed, transcellular clearance and F_g of multiple CYP3A4 compounds *via* end-point concentration measurements in TW monolayers has shown reasonable agreement with human *in vivo* values,[12] demonstrating the potential of organoids to model metabolic function.

Organoid-derived TW barriers and organ-on-chip systems grant apical and basal access while preserving multi-lineage cell type diversity, which makes them more suitable for permeability-metabolism studies compared with both organoids in domes and cell line-based *in vitro* models. However, these systems comprise a flat monolayer with limited spatial organization, failing to capture the crypt-villus architecture and cellular patterning of the real intestinal epithelium.[13] Furthermore, epithelial cells within TWs and organ-on-chip models adhere to stiff synthetic polymers instead of the softer extracellular matrix (ECM) of the native intestine. Others have demonstrated that intestinal organoids cultured on thick gradient crosslinked collagen scaffolds had enhanced drug metabolizing enzyme activity[14] and transporter function compared to parallel culture on conventional stiff TW inserts.[15]

In this work, we use newly developed bioengineered intestinal tissues to address several of the outstanding challenges of gut-on-chip systems for absorption and metabolism studies recently highlighted by Keuper-Navis *et al.* and pharmaceutical industry consortia.[16,17] The model comprises a luminally and basally accessible epithelial barrier, which is organized into crypt and villus-like domains, and features spatial patterning akin to that of the real intestinal epithelium. We characterized the presence of key small intestinal DTs and DMEs for drug screening applications and performed drug transport and inhibition studies, finding that the system performed similarly as in-house *in vitro* ADME (absorption distribution metabolism excretion) standards. Finally, we used *in silico* and *in vitro* modelling to estimate intestinal DMPK (drug metabolism and pharmacokinetics) parameters.[18] This new platform combines permeability assays with assessment of drug metabolism and provides new avenues to mechanistically model oral absorption of new drug candidates.

Results and discussion

Design and characterization of the bioengineered intestinal epithelium

The crypt-villus architecture of the intestinal epithelium is crucial for maintaining the function of the intestine including absorption of nutrients, barrier function, and metabolism.[13,19]

The heterogeneous morphology and higher crypt density and the presence of villi within *in vivo* tissue significantly extends luminal surface area enhancing drug absorption, lowering the apparent permeability of substances, and refines tissue regionalization. That architecture additionally encourages the maturation of enterocytes with high expression of DMEs and DTs. Simplified models are likely to underrepresent efflux effects due to faster saturation of DTs. However, it is challenging to replicate this complexity with the high reproducibility and high throughput required for drug screening. Prior research[20] demonstrated that extrinsic hydrogel patterning establishes repeatable epithelial architecture. This is achieved *via* mechanically mediated spatial gradients in YAP activity and Notch signaling, which promote the formation of crypt-like ($SOX9^+$ and $Ki\text{-}67^+$) and villus-like domains. We have recently developed next-generation bioengineered intestinal tissues that are luminally accessible, contain crypt-like domains and feature spatial patterning reflecting that of the crypt-villus axis.[20,21] Briefly, we use an elastomeric stamp with crypt-like projections to structure the surface of an ECM hydrogel with crypt topographies inside an in-house developed device, the OpenTop OrganoChip (Fig. 1A). Dissociated human small intestinal organoids derived from primary tissue are seeded on the hydrogel and allowed to form a confluent barrier which

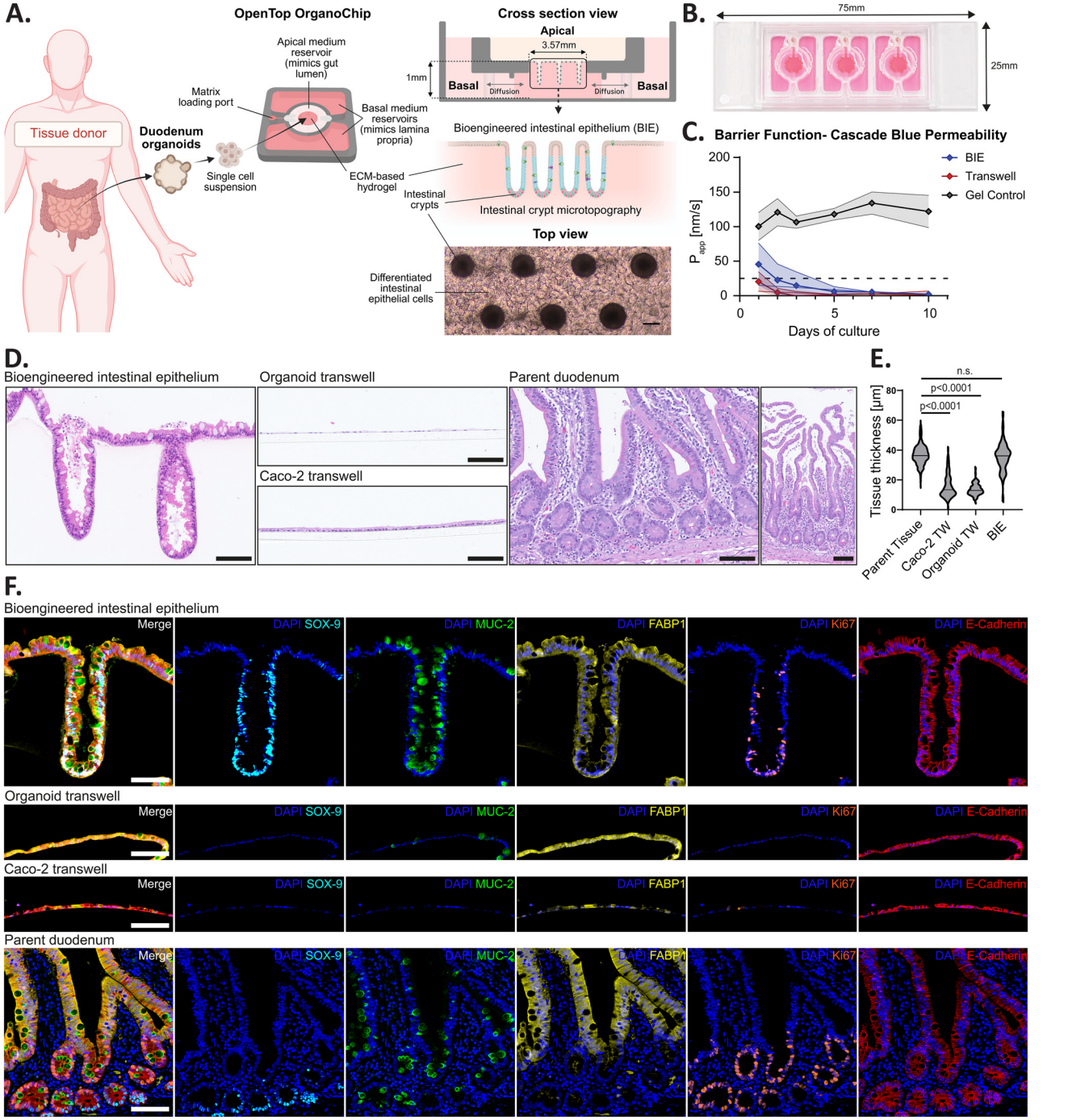

Fig. 1 Characterization of the bioengineered intestinal epithelium (BIE). (A) Schematic overview of the OpenTop OrganoChip (cross section) and generation of the BIE from duodenum intestinal organoids derived from donor tissue resections. After singularization of intestinal cells, the suspension is seeded onto the micropatterned hydrogel in the apical compartment of the OpenTop OrganoChip and forms a tight epithelial barrier with regionalization of crypt cells and differentiated enterocytes. Representative image of the formed BIE shown in bottom right, scale bar indicates 100 μm. (B) Image of the chip-slide in culture medium containing three separate chip units. (C) Measurement of barrier formation over time of culture on the OpenTop OrganoChip and standard 24-well transwells (TW), measured by the apparent permeability (P_{app}) of the 479 Da fluorescent tracer molecule Cascade Blue. The graph represents the average (±SD) of three chip units each of three organoid donor lines in independent experiments. A P_{app} value under 25 nm s^{-1} indicates complete barrier formation and is marked by a dotted line. (D) Representative hematoxylin and eosin (H&E) staining of cross sections of duodenum organoids on the OpenTop OrganoChip, on TW, Caco-2 cells on TW, and parent tissue at different magnifications. Scale bars indicate 100 μm. (E) Quantification of tissue thickness of parent duodenum tissue, duodenum organoids on the OpenTop OrganoChip, on TWs, and Caco-2 cells on TWs. Violin plots shown represent the mean (+distribution of data points) of >100 measurements from three different regions of interest. Data was analyzed by one-way ANOVA with subsequent multiple comparisons test, *p*-values are indicated on the graph, n.s. = not significant. (F) Representative cross section multiplex immunofluorescent (mIF) staining of duodenum organoids on the OpenTop OrganoChip, on TWs, Caco-2 cells on TWs, and donor-matched parent tissue sections stained against an epithelial (E-cadherin$^+$, red), stem (SOX9$^+$, blue), proliferating (Ki67$^+$, orange), secretory (MUC2$^+$, green), and absorptive (FABP1$^+$, yellow) intestinal cell marker. The scale bars indicate 100 μm.

conforms to the surface geometry, assuming the shape of periodically repeating crypts and inter-crypt (villus-like) domains (Fig. 1A and B). The bioengineered epithelium (BIE), comprising the epithelial barrier spread on the underlying patterned hydrogel, is housed within the OpenTop OrganoChip, which contains top- and side-reservoirs that grant luminal and basal access, respectively (Fig. 1A and B). To assess the barrier integrity of the established BIE and compare it to donor-matched 2D organoid monolayers grown in standard TWs, we monitored the permeation of the cell-impermeable fluorescent molecule Cascade Blue for 10 days following seeding (Fig. 1C). Even though initial variability between donor lines with regards to monolayer closure and barrier establishment was observed, all BIEs exhibited a tight barrier from day 5 onwards, marked by low paracellular permeability of the tracer molecule (P_{app} < 10 nm s^{-1}). In comparison, organoids on TWs established their barrier slightly faster. We selected cascade blue permeability assessment as quality control (QC) for subsequent drug permeability studies since it's a stable and sensitive functional measure of transcellular permeability, of relevant molecular size to approximate transport of small molecule compounds.

We next examined the morphological and cellular features of the BIE and compared them to existing approaches, including organoid- and Caco-2-derived TW monolayers. Our work focused on the duodenum for small molecule permeability and DMPK modeling, as it is the most relevant region of the small intestine. A recent report characterized how BIEs can reflect regional identity, including the differential expression of DMEs and DT, and modeling of the mucus layer.[21] We observed striking differences in epithelial thickness between BIE and organoids cultured in 2D on TW monolayers. Whereas both organoid- and Caco-2-derived TW monolayers exhibited a flat and spread epithelial morphology (thickness of ~15 μm), BIE barriers featured a thick, columnar morphology closely resembling that of the parental intestinal duodenum epithelium (thickness of ~40 μm) (Fig. 1D and E). Previous work has shown that differential cell spreading and crowding can control YAP activation, creating a crypt-villus-like axis.[20] When cells are seeded in a BIE, they accumulate within crypts, promoting cell proliferation and the formation of thick epithelial tissues. Another recent study demonstrated thick organoid monolayers on transwells, highlighting that optimal ECM coating significantly boosted cell growth and along with other precise culture adjustments.[7] Similarly, the stiffness and composition of the hydrogel that patterns BIEs is likely to contribute to increased cell proliferation and tissue thickness. Next, we evaluated the cell type composition and spatial patterning within the different intestinal models through multiplexed immunofluorescence analysis (Fig. 1F). Similarly to *in vivo* tissue, the SRY-box transcription factor 9 (SOX-9) positive stem and progenitor cells localized to the engineered crypt region in the BIE, marking a self-organized and regionally patterned stem cell niche, whereas in organoid and Caco-2 TW monolayers, SOX-9 staining could only be detected at low levels and scattered throughout the monolayer. Interestingly, the staining of antigen Kiel 67 (Ki67), which is used as an indicator of actively proliferating cells, can be found exclusively in the crypt compartment of the BIE, but is almost completely absent on the organoid TW and Caco-2 TW monolayers. Mucin 2 (MUC-2) staining, marking the goblet cell population, was strongly visible on the BIE on top of the chip area as well as in the crypt, but much more sparse on the organoid TWs and absent on Caco-2 TWs. Fatty acid-binding protein 1 (FABP1), which marks enterocyte populations, was detected strongly and evenly for BIEs and organoid TWs but was only very sparsely expressed in the Caco-2 TW.

The absence of Ki67 on organoid TW monolayers hints at a more actively proliferating epithelium in the BIE, which could also be retained for much longer culture periods than investigated in this study. This highlights a clear advantage of the use of organoids as BIE over culture on TWs, which lose their stem cell niche as well as active proliferating cells with longer cultivation time, and often the cell monolayer is easily damaged due to peeling from the plastic membrane of TWs. In comparison to the native tissue, the number of goblet cells is over-represented on the BIE, possibly due to the used medium composition that favors the differentiation into the secretory rather than the absorptive cell lineage.[22] The absence of mucin production in Caco-2 is a known disadvantage of the cell line, therefore modelling a mucus layer and evaluating its impact on drug permeation as a representation of the *in vivo* intestinal membrane is not possible in these cells. Co-culture with mucus-secreting HT29-MTX cells has been optimized for permeability studies, but is still not fully representative of the regionally different mucus compositions present in the gut.[23] A model that therefore supports representative *in vivo*-like mucus layer formation and informs about its impact on drug absorption could aid in drug formulation design, where no comprehensive model systems are yet available, especially for hydrophilic and physiologically unstable macromolecules such as peptides and proteins.[24–26]

DT and DME presence on organoid derived cultivation systems

In order to characterize the applicability of the BIE for permeability and drug metabolism studies, we stained for DTs P-gp and BCRP and the DME CYP3A4 (Fig. 2). For P-gp and BCRP, an apically located signal can be observed on the BIE as well as on the organoid and Caco-2 TW monolayers, reflecting the expression pattern of the native tissue. P-gp shows a more patchy expression throughout the monolayers in all systems compared to BCRP, while both colocalize with the apical-basal polarity marker villin. CYP3A4, which is the main enzyme responsible for metabolism of 30–50% of clinically used drugs,[27] is highly expressed on both BIE and organoid TWs, with a strong cellular expression in specialized cell types in the monolayer. In comparison to the native tissue, the staining is less uniform. In line with previous reports, Caco-2 cells do not show any staining for CYP3A4, unless they are genetically engineered.[28] Notably, for

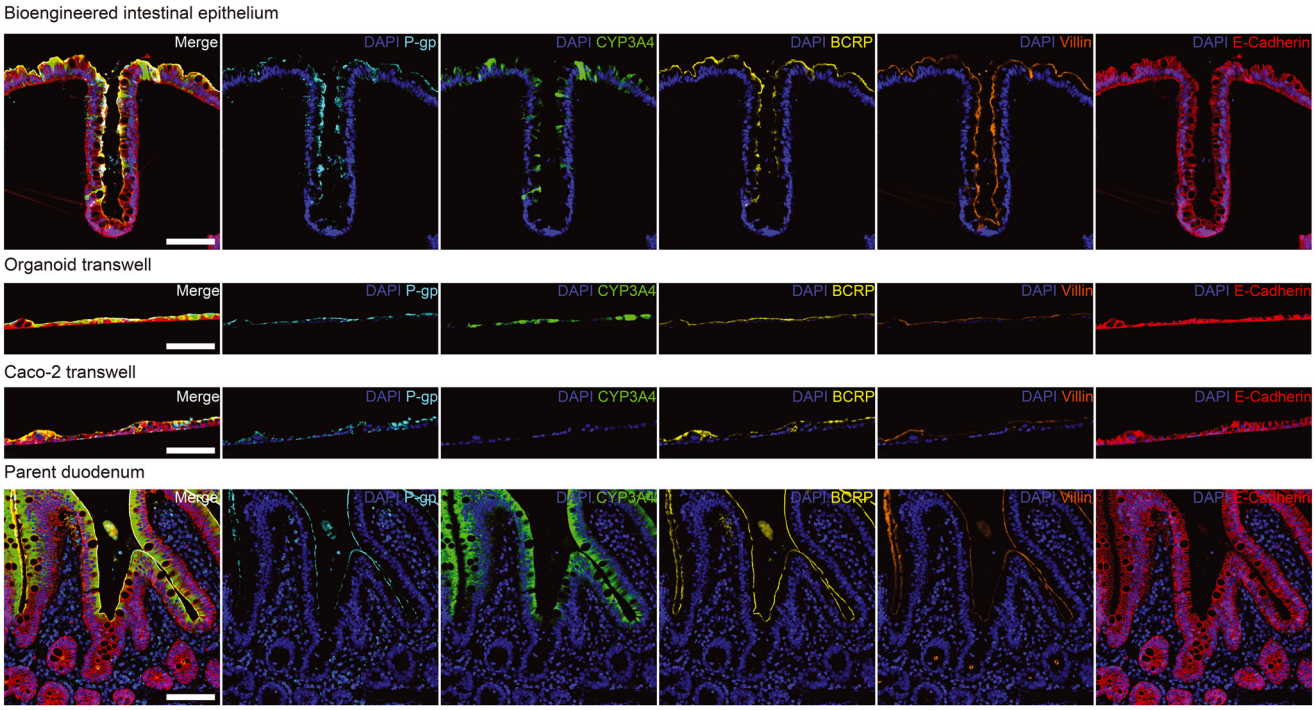

Fig. 2 Characterisation of DTs and DMEs in the BIE. Representative cross section multiplex immunofluorescent (mIF) staining of duodenum organoids on the OpenTop OrganoChip, on TWs, Caco-2 cells on TWs, and parent tissue sections stained against an epithelial marker (E-cadherin$^+$, red), DTs P-gp (blue) and BCRP (yellow), DME CYP3A4 (green) and the apical brush border marker villin (orange). The scale bars indicate 100 μm.

all three proteins, no expression can be found in the base of the crypt on the BIE harboring the stem cell niche, showing a clear regionalization of the differentiated cell population towards the upper crypt and surface of the hydrogel.

Taken together, BIE tissue organization and thickness closely resembles *in vivo* tissue with more accuracy than the same organoids cultured on TWs. Moreover, the retention of a stem cell niche and signs of active proliferation demonstrate potential for long-term culture, dynamic tissue remodeling, cellular crosstalk, and maturation. The presence of DTs and DMEs show promise for parallel measurement of intestinal drug permeability and metabolic function, where existing cellular models are unsuitable.

Transcriptomic characterization of drug transporters and drug metabolizing enzymes

To quantitatively determine an optimal timeframe for conducting drug transport and metabolism assays, bulk ribonucleic acid transcriptomic analysis (bulk RNA-seq) was used. Initial data acquired from BIE derived from a single donor across multiple days of culture revealed that the expression of key DTs was stable after 7 days of culture. For some DMEs such as CYP3A4, expression continued to increase with extended culture (Fig. S1). While BIEs maintain their stem cell niche, demonstrating epithelial turnover beyond day 10 and viability in culture for over 30 days (data not shown), barrier function is less reliable after 10 days. Given the practical benefits of shorter assay culture times, our focus was on this timeframe rather than longevity. Nevertheless, extending the culture period beyond 10 days would be advantageous for long-term or repeated dose toxicity studies, and for screening the sustained effects of tablet formulations and excipients. Therefore, day 7 and 10 were selected as optimal post-seeding time points for subsequent characterization and functional experiments for DTs and DMEs respectively.

Next, we benchmarked BIEs to other *in vitro* intestinal models and primary intestinal epithelium using bulk RNA-seq. In particular, BIEs created from three different donors were analyzed and compared to 1) 21 day Caco-2 TW monolayers as a widely used *in vitro* model for drug transport and barrier function assays, 2) donor-matched 3D organoids in domes and 3) donor-matched organoid-derived TW monolayers (Fig. 3A and B). To account for individual variability, we included samples from three different donors for dome culture, TW monolayers and BIEs. RNA from parent epithelial tissue for one of the donors was used as a benchmark for physiological gene expression. Fig. 3B displays volcano plots highlighting key differences observed between BIE and Caco-2 TW monolayers, organoids cultured in domes prior to BIE culture, and organoid TW monolayers. Diverse DMEs including CES2, CYP3A4, UGT1A1, UGT1A8 and UGT1A10 as well as goblet cell marker MUC2 were upregulated, and CES1 was downregulated within BIEs compared to Caco-2 monolayers (Fig. 3B and C). P-gp and BCRP were marginally upregulated in BIE. An extensive panel of genes corresponding to most relevant DMEs and DTs appears

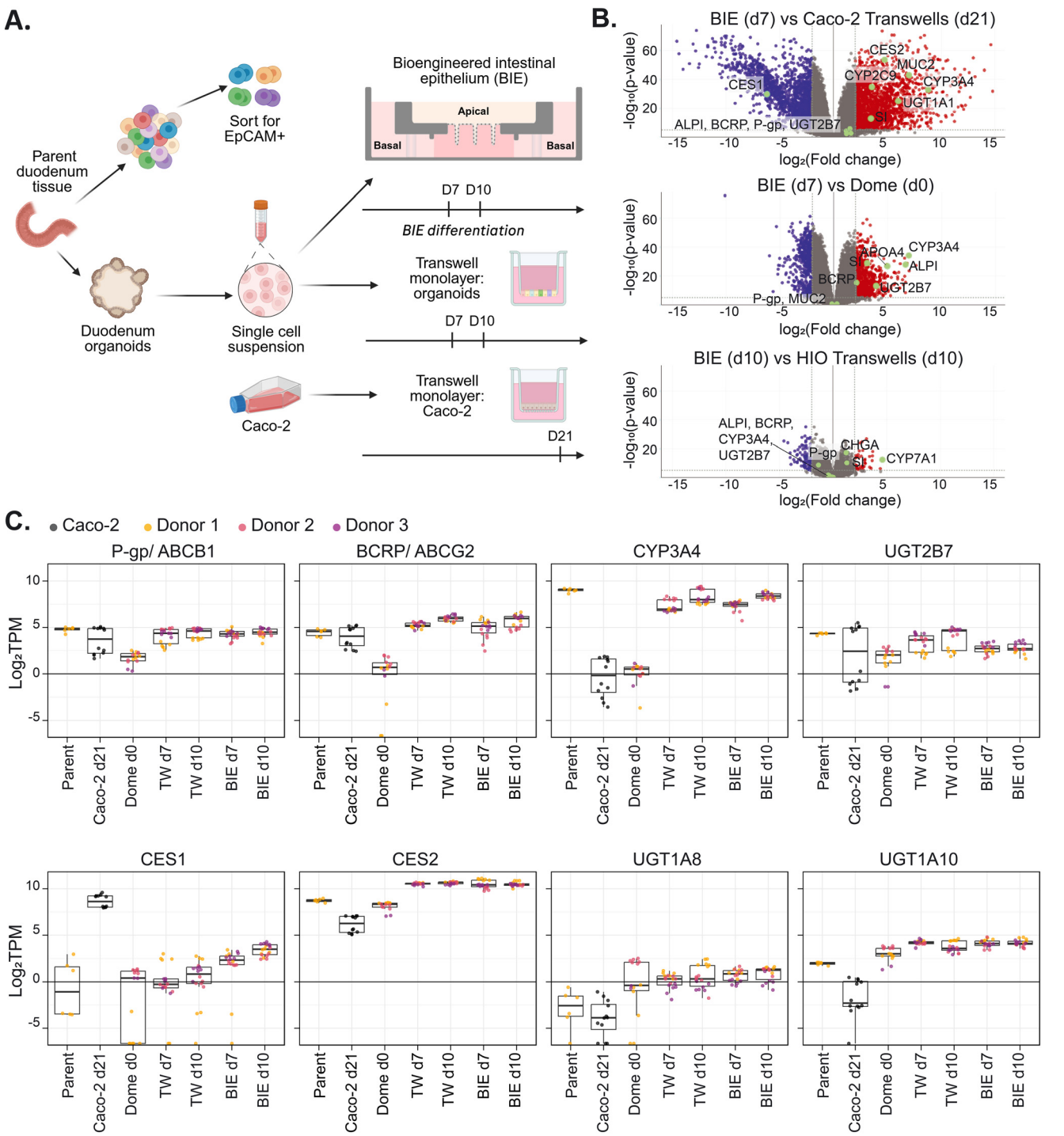

Fig. 3 Transcriptomic characterization of the BIE in contrast to parent tissue, dome culture (day 0), TW culture, and the Caco-2 cell line model (day 21). (A) Schematic of the experimental set-up. (B) Volcano plots contrasting BIE to Caco-2 TWs across all donors, donor-wise comparison of organoids before and after culture as BIE and donor-wise comparison of organoids cultured as a BIE against a classical TW culture with genes related to DTs, DMEs, and notable cell markers highlighted in green. Genes that are upregulated in BIE relative to each contrast appear in red with downregulated genes appearing in blue. (C) Box plots for specific genes of interest related to DTs and DMEs (P-gp, BCRP, CYP3A4, UGT2B7, CES1, CES2, UGT1A8, UGT1A10) displaying all contrasts in terms of $\log_2$ TPM (transcripts per million). Technical replicates appear as individual data points representing separate BIE and TW monolayer samples, with separate donor lines (biological n = 3) appearing in different colors and Caco-2 samples appearing in black. For technical replicates: all BIE, organoid TW, and donor 1 parent samples N = 6; for Caco-2 TWs N = 12; and dome cultured samples N = 2–6.

in Fig. S2. The presence of intestinal DMEs and mucus secreting cells within the BIE offers additional opportunities for metabolism and permeability assessment compared with Caco-2 monolayers, which appear to be suitable for modeling

transport alone. Comparing BIE to 3D organoids, which have previously been used to model intestinal metabolism,[5] we noted significantly upregulated expression of CYP3A4 and mature enterocyte markers APOA4, SI and ALPI within BIE. These data suggest that organoid-derived barriers are more suitable for metabolism assessment compared with conventional organoids in domes. We did not observe substantial gene expression differences between BIE and organoid-derived TW monolayers, suggesting similar functionality and suitability for drug transport and metabolism assessment between these two models.

Assessment of passive permeability and drug transporter functionality

Having assessed the expression of genes pertinent to epithelial maturation and transport across the barrier within the BIE, we set out to evaluate the functionality of the model. In particular, we investigated whether the BIEs captured the passive and active permeation of different types of control compounds. In addition to the bioengineered intestinal tissues themselves, the design of the OpenTop OrganoChip housing them facilitates permeability assessments. The central apical reservoir represents the intestinal lumen and can be used to mimic oral delivery of compounds. Molecules that are applied to either side of the barrier can cross the epithelial monolayer as well as permeate through the ECM compartment of the OpenTop OrganoChip and diffuse into the adjacent reservoirs, from which they can be collected and quantified to determine the permeated fraction. The hydrogel compartment, consisting of a collagen I/basement membrane extract (Matrigel) mix, serves as an essential scaffold that supports cell adhesion and guides organization of seeded organoids. However, it may also interact with and sequester molecules crossing the barrier, thereby influencing their diffusion into the medium reservoirs and ultimately affecting permeability assessments. In order to investigate if this hydrogel compartment poses a permeation barrier to small molecules, diffusion through the OpenTop OrganoChip was modelled using finite element simulations and compared to measured values from the hydrogel containing platform in the absence of cells. The small fluorescent tracer molecule Cascade Blue was used in the simulation for comparison with experimental data, since its molecular weight of 479 g mol^{-1} is in a similar size range of most small molecules developed for oral delivery.[29] When assuming the diffusion coefficient of the hydrogel matches the equivalent volume of water, the experimental data fits closely with the simulated diffusion dynamics on the cell-free OpenTop OrganoChip (Fig. S3). The alignment of experimental data to the simulation indicates that the porosity of the hydrogel compartment causes negligible hindrance to the diffusion of small molecules such as Cascade Blue. Larger molecular weight molecules with different physicochemical properties could not be simulated with this methodology and should be further validated.

Many prototype organ-on-chip systems have provided unreliable results when applied to the study of drug molecules due to drug adsorption and absorption by the fabrication materials. The advantage of the microfluidic device used in this study over commonly used polydimethylsiloxane (PDMS)-based systems is the usage of cyclic olefin copolymer (COC), which is known for its low absorption and adsorption behavior.[30–33] Since mass balance of all tested compounds in this study showed a recovery of >85%, adsorption to as well as absorption into COC can be excluded.

Having confirmed the usability of the platform with regards to material properties, we next set out to investigate passive permeability and drug transporter activity within the BIE. Since the system exhibited physiologically relevant expression of the main intestinal transporters that affect drug absorption, we considered a panel of compounds with known apparent permeability (P_{app}) and tested their passive permeation as well as transporter-mediated efflux behavior in the BIE. We included a moderate passively permeable compound (atenolol), a high passively permeable compound (propranolol), a P-gp substrate (edoxaban), and a BCRP substrate (2-amino-1-methyl-6-phenylimidazo[4,5-*b*]-pyridine (PhIP)).[34–37] The respective biopharmaceutics classification system (BCS) class, molecular weight, fraction absorbed (% Fa, if known), as well as their DT interaction can be found in Fig. 4A. After cultivating duodenum BIEs on the OpenTop OrganoChip for 7 days, the four compounds were each added to either the apical (A) or basolateral (B) side and incubated for 3 hours before the acceptor compartment on the opposing side of the intestinal barrier was analyzed for its respective compound concentration (Fig. 4B). For both atenolol and propranolol, equal apparent permeability values were observed for both directions (A → B and B → A), with atenolol showing close to 4-fold lower passive permeability than propranolol, which is in line with existing data.[38,39] For edoxaban and PhIP, a clear asymmetry in transport was observed, with a significant efflux of compound towards the apical compartment. Both edoxaban and PhIP showed an efflux ratio (ER) value >2, indicating an active transport of molecules to the apical compartment (Fig. 4C). To further investigate if the observed efflux of edoxaban and PhIP can be related to specific DT activity, selective inhibitors for P-gp (zosuquidar) and BCRP (Ko143) were added to the medium. Addition of zosuquidar did not affect the permeability of atenolol and propranolol, as expected for the two passively permeating compounds. However, efflux was abolished for edoxaban and PhIP in presence of zosuquidar and Ko143, respectively, leading to equal apparent permeability from A → B and B → A for both compounds (Fig. 4D).

These results demonstrate the specific inhibition of P-gp and BCRP in our BIE, indicating functional DT expression and localization within the system. We note that edoxaban exhibited variability in ER between the individual BIE donors (ER = 6.3, 60% CV), whereas the ER values of PhIP were consistent across donor lines (ER = 3, 28% CV). This observation might stem from different P-gp protein levels originating from donor-inherent differences in expression levels, which have been observed in

A.

Compound	Permeability	Molecular Weight [g/mol]	BCS class	Fraction Absorbed [%]	Transporter substrate
Atenolol	moderate	266.3	III	52	no
Propranolol hydrochloride	high	295.8	I	90	no
Edoxaban	low	548.1	IV	n.a.	P-gp
PhIP	moderate	224.3	n.a.	n.a.	BCRP

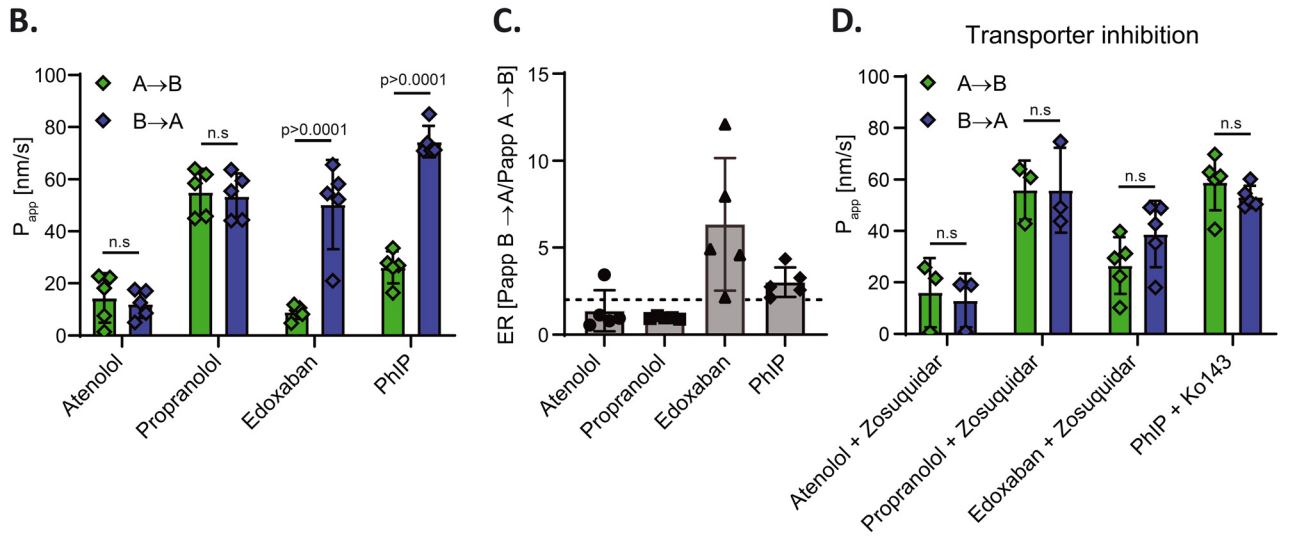

Fig. 4 Application of the BIE for drug permeability assessment. (A) Compounds used in this study with their respective BCS classification, molecular weight, and fraction absorbed data (% FA, n.a. = no clinical data available). (B) Human duodenum organoids were cultured as BIE for 7 days and bidirectional apparent permeability of atenolol (25 μM), propranolol (1 μM), edoxaban (1 μM), and PhIP (1 μM) for 3 hours was measured. (C) ER was calculated from data in (B), dotted line indicates ER of 2. (D) Inhibition of DTs P-gp and BCRP was tested by cultivating human duodenum organoids as BIE for 7 days and performing a 3 hour bidirectional permeability assay with atenolol (25 μM), propranolol (1 μM), and edoxaban (1 μM) in the presence of 1 μM zosuquidar, or PhIP (1 μM) in the presence of 1 μM Ko143. Each datapoint represents the average of three chips cultivated with cells from one donor. 3–5 different donor lines were tested, values shown represent the mean (±SD) of 3–5 independent experiments. Data was analyzed by 2-way ANOVA with subsequent Bonferroni's multiple comparisons test (B and D), *p*-values are indicated on the graph, n.s. = not significant.

tissue resections and functional *in vivo* studies before.[40,41] Besides interindividual differences, the intraindividual variability in DT levels that are present in different regions of the gut pose an exciting area of research and could aid in understanding regional absorption in the intestinal tract that can inform formulation strategies in oral drug delivery. Taken together, these findings indicate a mature intestinal epithelium when cultured as a BIE, with functional and specific DT activity that can reflect the permeation behavior of different compounds and has a high potential to be used as a platform for drug permeability testing.

Application of BIEs for Intestinal ADME assessment

Parameters derived from *in vitro* or animal *in vivo* experiments are used to predict human pharmacokinetics and DDI (drug–drug interaction). Currently, to predict F_g *in silico*, data from separate *in vitro* systems are combined within modelling approaches to estimate orally administered drug absorption and intestinal metabolic clearance as initial steps prior to hepatic metabolism and systemic distribution. Given the presence of key intestinal DMEs, DTs, and apical/basolateral accessibility in addition to the barrier characterization detailed above, we proposed the application of the BIE in intestinal absorption and metabolism studies.

Metabolic activity of CYP3A4 was confirmed in BIEs and TW monolayer equivalents using a lucuferin-based substrate for rapid luminescent quantification (Fig. 5A). Both TW and BIEs demonstrated elevated activity after rifampicin induction, which could be inhibited with ketoconazole, confirming the expected metabolism induction and inhibition characteristics of CYP3A4 in the system. One of the three donors was less responsive to

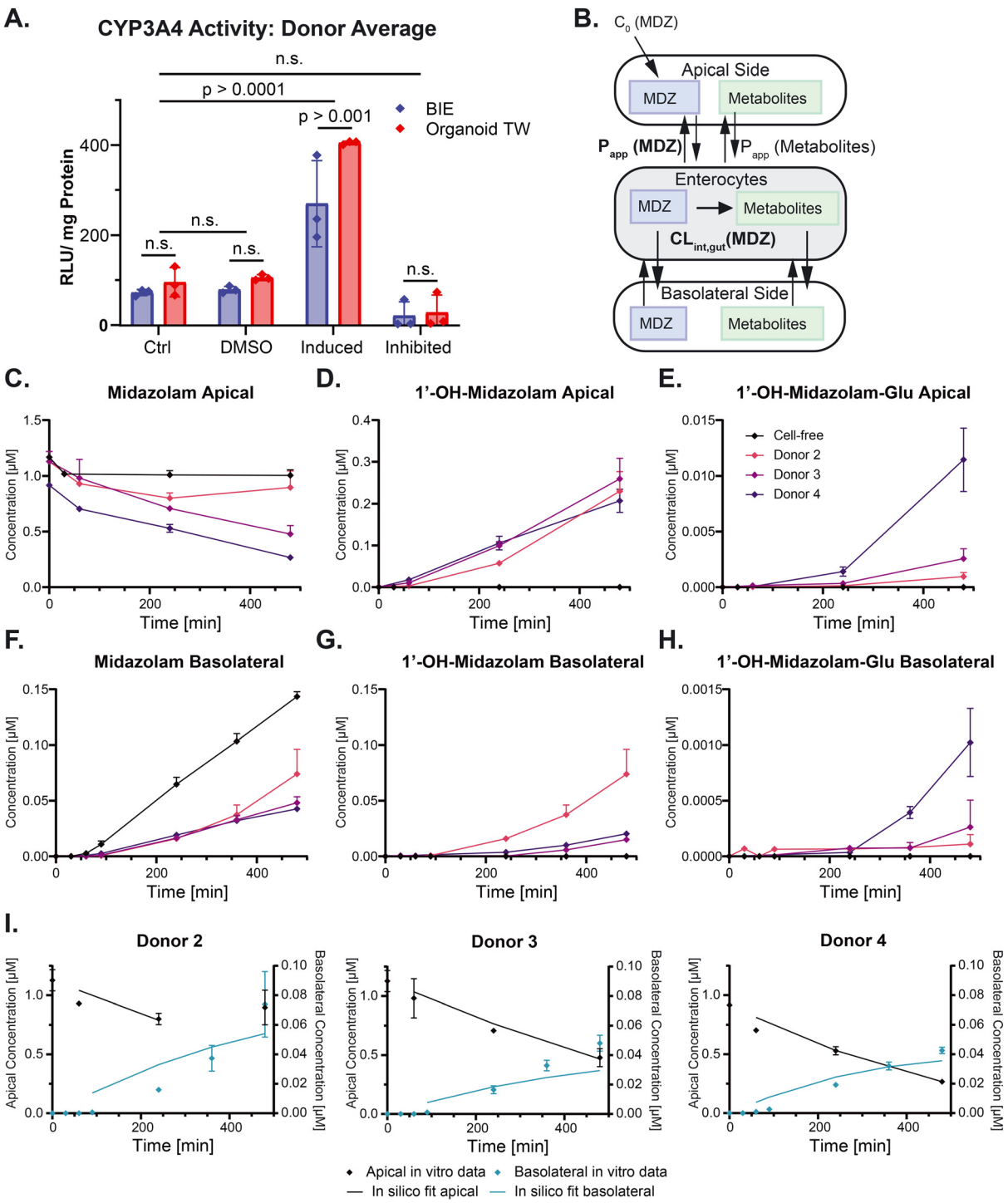

Fig. 5 Application of a BIE for determining intestinal absorption and metabolism parameters demonstrated with midazolam. (A) CYP3A4 activity was confirmed on the BIE and organoid TW monolayers with a pro-luminescent probe substrate normalized to tissue protein content after 10 days of parallel culture with induced (rifampicin) and inhibited controls (rifampicin, followed by ketoconazole). 3 donor lines were assessed with bars representing the average and standard deviation across the donors and each point displays the average of 3 technical replicates for each donor. Data was analyzed *via* Bonferroni's multiple comparisons test and Šídák's multiple comparisons test, with *p*-values indicated and n.s. = not significant. (B) Compartmental model used in the silico experimental design for the conversion of midazolam to 1′-OH-midazolam within the culture system (further conversion to 1′-OH-midazolam-glucuronide not shown due to space constraints). The midazolam study was performed on day 10 of culture in 3 duodenum donor lines and a cell-free control. Time-concentration profiles of midazolam (MDZ) and its metabolites 1′-hydroxymidazolam (1′-OH-MDZ) and 1′-hydroxymidazolam glucuronide, (1′-OH-MDZ-Gluc) were determined apically (C–E) and basolaterally (F–H), respectively. For (C–H) colours represent the different donors, and the sampling points presented as the average and standard deviation of 3 technical replicates. (I) The *in silico* model fit to experimental data estimates DMPK parameters for each organoid donor. Apical data appears in black and corresponds to the left *y* axis, basolateral data appears in blue and corresponds to the right y axis. *In vitro* data was collected in triplicate and is displayed as average with error bars representing the standard deviation.

inhibition and more responsive to induction, which could reflect greater activity from other CYP enzymes in that donor. Between BIEs and organoids cultured on TWs the CYP3A4 activity measured was comparable, aside from under induction conditions where TW culture had higher measured activity.

Midazolam is extensively used *in vitro* and *in vivo* for predicting CYP3A-mediated drug–drug interactions (DDIs) and is recommended as a test compound for intestinal CYP3A4 activity.[17,42] CYP3A4 is the key DME in the small intestine responsible for the phase I bioconversion of midazolam to its primary metabolite 1′-hydroxymidazolam. Further phase II glucuronidation by UGT enzymes including UGT2B7 and possible drug transporter interaction with midazolam is additionally thought to occur *in vivo*.[43] We used the BIEs to simultaneously investigate intestinal permeability and metabolic clearance of midazolam. Computational modeling complemented the BIE-based experimental approach in two capacities: 1) to guide the experimental design and 2) to estimate F_g – the fraction of midazolam escaping intestinal metabolism. We previously described a compartment-based *in silico* model that could simulate the concentration-time profiles of midazolam and its metabolites (Fig. 5B).[3] *In silico* design of experiments determined the timing of a finite number of experimental concentration samples that would ultimately allow F_g estimation. It accounted for LC-MS/MS detection sensitivity, volume constraints for bioanalysis, the OpenTop OrganoChip apical and basolateral volume, evaporation rate and BIE cell number (Fig. S4 and S5). After simulating the experiment over a 25 hour period, we determined that an 8 hour experiment would capture the data points required to estimate dynamics of the entire concentration-time profile.

Midazolam was added to the apical compartment of the BIE, with apical and basolateral samples collected and measured *via* LC-MS/MS to determine the concentration of midazolam and two of its key metabolites at the times specified in Table S7. The apical concentration-time profiles from three different patient-derived organoid lines and a cell-free control are presented in Fig. 5C–E with basolateral counterparts in Fig. 5F–H. The cell-free control indicates the rate at which the parent molecule passes through the hydrogel scaffold without cells present, showing no spontaneous conversion into either of the metabolites (Fig. 5D, E, G and H). Conversely, in the presence of a BIE, the midazolam concentration drops in the apical side, with less of the compound appearing in the basolateral side, and a significant proportion metabolized to 1′-OH-midazolam by CYP3A4. The apical and basolateral 1′-OH-midazolam concentration-time profiles (Fig. 5D and E) indicate a bias towards apical side, suggesting active efflux, whereas the detection of 1′-OH-glucuronide demonstrates functional activity of UGT enzymes, such as UGT2B7. Whilst there is some variation in enzyme activities between donors, the overall pattern of metabolism in each compartment is repeatable. Notably, donor 4 has significantly higher production of the secondary metabolite in the apical and basolateral compartments (Fig. 5E and H). Interestingly, it was also this donor that was less responsive to ketoconazole inhibition in Fig. 5A. The appearance of primary and secondary metabolites across all three organoid lines indicates consistent CYP3A4 and UGT activities. It was not possible to complete this intestinal DMPK study in TW organoid monolayers for all the donors presented in Fig. 5C–H due to a high incidence of monolayer peeling. This highlights that combining pre-existing platforms with organoid-derived epithelial models can present technical challenges. In this application we found BIEs to be more robust than equivalent organoid TW models.

Table 1 Parameter estimates for the mechanism-based pharmacokinetic model of midazolam in BIE across 3 different patient-derived organoid lines

Donor	2	3	4	Average
Passage	8	7	11	—
CL_{int} (MDZ) [μL $min^{-1}/10^6$ cells]	8.71	21.1	23.5	17.6
P_{app} (MDZ) [nm s^{-1}]	80.2	74.3	110	88.0
F_g	0.67	0.46	0.43	0.52

Lastly, we fitted the *in silico* model to the experimental time-concentration data to determine the intrinsic clearance and apparent permeability (Table 1) that were subsequently used in the Q_{gut} model to estimate F_g.[4,44] The average values determined for intrinsic intestinal clearance (CL_{int}) and corresponding F_g values fall around the range determined with primary intestinal mucosa (CL_{int} = 16.9 ± 3 μL $min^{-1}/10^6$ cells; F_g = 0.55 ± 0.04 (ref. 4)). *In vivo* F_g measured values show an even greater standard deviation of 0.55 ± 0.1.[4] Overall, this demonstrates the potential to use one *in vitro* system to model three interconnected intestinal ADME processes: phase I oxidative metabolism, phase II glucuronide formation and active efflux of the primary metabolite.

The current study provides a baseline characterization and validation of a novel *in vitro* tool for screening intestinal drug transport and metabolic disposition, benchmarked against current pharmaceutical industry gold standards and, where feasible, *in vivo* controls. We demonstrate the utility of *in silico* modeling to optimize experimental design and quantitatively estimate intestinal ADME parameters, as a complementary New Approach Methodologies (NAMs) strategy. The culture of BIE was found to offer enhanced handling robustness for drug transport studies and technical reproducibility compared to organoid TW monolayers. With healthy organoid lines that have undergone QC, currently we achieve a 90% yield in forming BIEs with appropriate barrier function for compound studies. The robust tissue patterning of crypts with a retained stem cell niche and actively proliferating cells presents the added potential for compound experiments requiring extended culture durations or multiple dosing strategies. Moreover, the presence of secretory cells opens avenues to explore the effects of mucus on drug permeation. With further experimental validation, including validation of other metabolic pathways such as CYP2C9 and CES2, mechanistic modeling could be employed to extract additional quantitative intestinal ADME parameters that existing *in vitro* systems are unable to assess such as phase II

metabolite intrinsic clearance and the efflux ratio of metabolic products. We saw a bias towards the concentration of 1′-OH-midazolam in the apical side which suggests active efflux, consistent with what was observed in a similar model.[11] The ability to screen interconnected metabolic and permeation behaviors would be particularly valuable for screening the gut extraction of oral prodrugs.

For translation to *in vivo* data, further efforts could be directed at establishing a regression model between *in vitro* P_{app} and *in vivo* P_{eff} data for compounds with a known range in P_{eff} similar to Tanaka *et al.*[7] It would be worthwhile to optimize incubation buffer conditions to balance minimal compound binding, with the option for extended assay incubation time, and performance of the microtissue, prioritizing barrier and metabolic function whilst keeping in mind what is representative of physiological conditions. For large scale compound studies, automation of BIE maintenance, experimental set-up and sample collection could minimize human labor costs and the risk of human error. Further work should additionally focus on characterizing what is reflective of patient diversity, different regions of the intestine, how organoid handling in establishing and biobanking lines may contribute, or if there are patterns in donors such as age, gender, race, or medical history.

Material & methods

Human samples

Human intestinal tissue samples and annotated data were obtained from the non-profit foundation HTCR (Munich, Germany). The framework of the HTCR Foundation has been approved by the ethics commission of the Faculty of Medicine in the Ludwig Maximilian University (no. 025-12) and the Bavarian State Medical Association (no. 11142). Consenting patients underwent visceral surgery with partial resection of small intestine for various oncologic indications and tumor-free regions of biopsies were used for generation of organoid lines and single cell suspensions for RNA sequencing. Basic donor demographic information is listed in Table S1.

Generation and cultivation of intestinal organoids

Received tissue resections from HTCR were first washed with phosphate buffered saline (PBS) (Gibco) containing penicillin/streptomycin and Primocin. Underlying muscularis as well as serosa and fat were removed using fine scissors. The mucosal layer was then scraped with a microscopy slide to remove excess mucus as well as villus structures. The resulting mucosa was incubated in ice-cold PBS + 10 mM EDTA for 30 minutes on a shaker. To isolate the crypts, the tissue was then transferred to advanced DMEM-F12 (Gibco) + 1% bovine serum albumin (BSA) (Gibco) and scraped again. The extracted crypts were centrifuged, washed with advanced DMEM-F12 + 1% BSA and resuspended in small Matrigel (Corning) droplets. After polymerization of the domes at 37 °C, organoid culture medium was added, containing advanced DMEM/F12, 1× glutamax (Gibco), 1% penicillin/streptomycin (Gibco), 10 mM HEPES (Gibco), 2% Rspo3-Fc fusion protein conditioned medium (IpA), 2% Noggin-Fc fusion protein conditioned medium (IpA), 1× B-27 supplement minus vitamin A (Gibco), 1 mM *N*-acetylcysteine (Sigma), 50 μg ml^{-1} Primocin (InvivoGen), 100 ng ml^{-1} recombinant human IGF-1 (BioLegend), 50 ng ml^{-1} recombinant human FGF-2 (Peprotech), 50 ng ml^{-1} recombinant human EGF (Peprotech), 500 nM A83-01 (Tocris), 0.15 nM Wnt Surrogate-Fc Fusion Protein (IpA) and freshly supplemented with 10 μM Y-27632 (Tocris) for the first two days of culture.[22] Organoids were cultured at 37 °C, 5% CO_2, 95% humidity and passaged every 5–7 days by incubating with gentle cell dissociation reagent (Stemcell Technologies) for 12 minutes, washing 1× with advanced DMEM/F12 supplemented with 1× glutamax, 1% pen/strep and 10 mM HEPES (base medium) and breaking by strong up and down pipetting. After re-seeding in Matrigel domes, the culture medium was supplemented with 10 μM Y-27632 for the first two days of culture.

$EPCAM^+$ cell sorting of native tissue for RNA-sequencing

The intestinal tissue was cleaned as detailed above. The resulting mucosa was transferred to a Petri dish and kept wet using a minimal amount of base medium supplemented with 50 μg ml^{-1} Primocin. The tissue was then finely cut into very small pieces using scissors, collected and transferred into a gentleMACS C Tube containing a pre-prepared enzyme mix and digestion media (Miltenyi, 130-095-929). The tube was then inserted into the gentleMACS™ Octo Dissociator, with the digestion protocol Soft 37C_h_TDK_1. Upon completion, 10 mL of cold base medium was added to the tube, and the resulting digest was strained using a 100 μm pluriStrainer (PluriSelect). The collected cells were centrifuged at 350*g* for 10 minutes at 4 °C to pellet the cells. Cells were counted and stained with EpCAM – APCVio770 (Miltenyi, 130-111-002), CD45 – BV510 (Biolegend, 103137) and Zombie UV (Biolegend, 423107) for viability. $EpCAM^+$ cells were sorted based on singlet selection, $ZombieUV^-/EPCAM^+/CD45^-$ on an Aria Fusion into cold base medium. Resulting cells were spun down, counted and lysed in MagNA Pure lysis buffer (Roche) in replicates of six.

Caco-2 cell culture

Caco-2 cells were obtained from ATCC (HTB-37) and cultured in DMEM + glutamax medium (Gibco) containing 1% penicillin/streptomycin, 10% fetal bovine serum (Gibco) and 1% non-essential amino acids (NEAA) (Gibco) at 37 °C, 5% CO_2 and 95% humidity. Upon reaching 80% confluency, cells were split by adding TrypLE Express Enzyme (Gibco) for 10 minutes. For TW culture, cells were seeded at a density of 1×10^5 cells per TW (Greiner-ThinCerts, 24-well, 0.4 μm pore size) and cultured for 21 days with media exchange every 2–3 days.

Preparation of the microfluidic device and cell seeding

The micropatterned organ-on-chip device used in this study was designed in-house and produced by injection molding using cyclic olefin polymer. It consists of a middle chamber with a

loading port for hydrogel loading and micropatterning, an apical chamber used for seeding intestinal organoids onto the micropattern, and two adjacent basal chambers flanking the hydrogel compartment separated by pillars to avoid hydrogel outflow.[21] The chip is designed in a standard slide format (75 × 25 mm), containing three independent chips per slide. To increase throughput and enable automation workflows, we developed a slide-to-plate converter that allows four slides to be snapped into a standard cell culture plate format, thus creating a 12-chip plate. Large-scale chip production is outsourced to an external manufacturing facility. Corresponding authors can be contacted to discuss collaborations and obtain chip samples. For hydrogel loading, the loading port and middle chamber were pre-coated with 1 mg ml^{-1} dopamine hydrochloride (Sigma Aldrich) in 20 mM Tris HCl pH 8.3 overnight at 4 °C. The chips were then washed 3× with deionized water, dried and UV sterilized for 1 hour. Extracellular matrix (ECM) consisting of 25% (v/v) Matrigel (Corning) and 75% (v/v) neutralized 6 mg ml^{-1} bovine TeloCol®-6 type I collagen solution (Advanced Biomatrix) was then loaded through the loading port against an inserted PDMS stamp containing the inverted micropattern and polymerized at 37 °C for a minimum of 10 minutes. The micropattern used in this study contained an array of microwells mimicking the geometry of intestinal crypts with 650 μm depth and a slightly conical shape ranging from 70 to 120 μm in diameter (bottom to top). For seeding of the OpenTop OrganoChip, human duodenum organoids between passage 5 and 15 were removed from Matrigel domes four to five days after the last split, washed at least once with base medium and dissociated with TrypLE express solution (Gibco) containing 250 U ml^{-1} DNaseI (Roche) and 10 μM Y-27632 (Tocris) for 8–15 min at 37 °C. After singularization, cells were diluted in base medium containing 1% BSA (Miltenyi) and 10 μM Y-27632 and subsequently passed through a 40 μm strainer (PluriSelect). The cells were pelleted, resuspended in culture medium without A-83 supplemented with 10 μM Y-27632 and 1–1.5 × 10^5 single cells were seeded onto the micropatterned hydrogel in the apical chamber. Medium was exchanged every other day, with the addition of A-83 on day 2–4 (after full monolayer formation) and removal of EGF after 4 days of culture.

Barrier integrity assessment with Cascade Blue

To assess barrier integrity on the BIE and TW, the cells were washed once with advanced DMEM/F12 supplemented with 1× glutamax, 1% pen/strep and 10 mM HEPES. After removing the wash medium thoroughly from all compartments, 100 μl of a 10 μM solution of Cascade Blue hydrazide, trilithium salt (Invitrogen) in culture medium was added to the apical compartment of the OpenTop OrganoChip/TW and the basal compartments were filled with a total of 300 μl of culture medium (distributed equally to both basal compartments). After 3 hours of incubation at 37 °C, 5% CO_2 and 95% humidity the fluorescence of the basal medium was measured against a standard curve on the Flex Station 3 plate reader at 380 nm excitation and 420 nm emission. The measured concentrations were used to calculate the apparent permeability (P_{app}) using eqn (1) and a value under 25 nm s^{-1} was considered an intact, tight barrier.

$$P_{app} = \frac{V_{acc} \times dC_{acc}}{A \times dt \times C_{don,t=0}} \quad (1)$$

where V_{acc} is the volume of the acceptor compartment, dC_{acc} is the concentration in the acceptor compartment over the time of the experiment, A is the surface area of the hydrogel, dt is the time that the experiment was run for and $C_{don,t=0}$ is the concentration of the compound in the donor compartment at the start of the experiment.

Bulk RNA-sequencing characterization

1.) Library prep. Cell pellets were resuspended in 350 μL Magna Pure External Lysis Buffer (Roche, 06374913001) and stored at −80 °C. RNA was extracted using the Magna Pure 96 instrument (Roche) and the Magna Pure 96 Cellular RNA Large Volume kit (Roche, 05467535001). RNA was quantified using the Qubit RNA HS assay (Invitrogen, cat# Q32852). The RNA integrity number (RIN) scores were determined by using the TapeStation 2200. For this, the High Sensitivity RNA screen tape (Agilent, cat# 5067-5579) and the High Sensitivity RNA ScreenTape Sample Buffer (Agilent, cat# 5067-5580) were used, following the manufacturer's instructions. RNA library preparation was performed using the Illumina stranded mRNA Prep (Illumina, cat# 20040534), according to the manufacturer's protocol. A total of 200 ng RNA was used for all libraries as input material. Final Library PCR amplification was done using 12 cycles. Prepared libraries were quantified using the Qubit 1× dsDNA HS kit (Invitrogen, cat# Q33231) and checked for fragment size distribution using the TapeStation 2200 using the D1000 DNA screen tape (Agilent, cat# 5067-5582) with D1000 Reagents (5067-5583). The quantified libraries were pooled in equimolar amounts and sequenced on the NovaSeq 6000 system with 2 × 50 bp paired-end (PE) reads, targeting 50 million PE reads per library.

2.) Data pre-processing. Raw sequencing data underwent base calling using bcl-convert (v4.3.13, Illumina). The quality of the resulting FASTQ files was assessed using FastQC (v0.12.1). Adapter trimming and quality filtering were performed with fastp (v0.23.4)[45] using default parameters. Paired-end RNA-seq reads were aligned to the GRCh38.p14 build of the human genome using STAR aligner (v2.7.11b)[46] with default mapping parameters. Gene-level quantification was performed using featureCounts from the Subread package (v2.0.6)[47] based on the Ensembl v112 reference annotation, with parameters set to exclude low-quality mapping reads (−Q 10) and perform strand-specific quantification (−s 2). Quality control metrics were generated using samtools stats (v1.19.2),[48] Picard CollectRnaSeqMetrics (v3.1.1) (**https://broadinstitute.github.io/picard/**), and RSeQC (v5.0.3)[49] (bam_stat.py and infer_experiment.py). Results were aggregated and visualized using MultiQC (v1.21).[50] To help correct the observed batch effects

introduced from data originating from two distinct sequencing runs, the counts were adjusted using the ComBat_seq method from the bioconductor SVA R library version 3.48.0.[51]

3.) Differential gene expression analyses. The batch effect corrected gene counts were then first verified for quality control measures to detect other potential known confounding factors which were factored in as covariates in the statistical model. The differential gene expression analysis was carried out using voom-limma[52] a to yield gene level dysregulation between the conditions tested.

Histology & immunofluorescent staining

1. FFPE embedding of BIE. Chips were washed once with 1X DPBS before fixation with 4% paraformaldehyde (PFA) in the chip-slide. After 30 min of fixation at RT, the chips were washed three more times before using a biopsy puncher (3 mm diameter) to detach the biological material from the chip. In parallel, the chip histoarray, specifically designed to facilitate co-planar embedding of up to 50 chips, was prepared according to Harter *et al.*[53] Briefly, liquid histogel was dispensed into the chip-histomold and allowed to polymerize for 20 min at 4 °C. Following polymerization, the histoarray was demoulded. Chips were then transferred with a thin tweezer into the slits of the histoarray. After careful glueing of the chips in the wells of the histoarray, the histoarray was filled and distributed into biopsy cassettes. Samples were dehydrated overnight using a vacuum filter processor (HistoCore PEARL, Leica). The following day, samples were embedded in liquid paraffin.

2. Microtome sectioning. Formalin fixed paraffin embedded (FFPE) blocks were sectioned at a thickness of 3.5 μm and transferred on Superfrost Ultra Plus Gold Adhesion Slides. Slides were incubated in a slide oven overnight at 37 °C.

3. H&E staining. H&E staining was performed using the standard protocol on a Ventana HE600 stainer (Roche Tissue Diagnostics). H&E-stained slides were digitized with a brightfield scanner at ×40 (Hamamatsu, NanoZoomer; pixel size 0.23 μm px^{-1}).

4. FFPE-based mIF staining. As previously described,[53] Opal mIF staining of FFPE slides was performed using a Ventana Discovery Ultra automated tissue stainer (Roche Tissue Diagnostics). The slides were baked for 8 minutes at 60 °C, followed by a deparaffinization cycle for 8 min at 69 °C (deparaffinization cycle repeated three times). Heat-induced antigen retrieval was performed with Tris-EDTA buffer (pH 7.8, CC1, 950-227, Ventana) at 95 °C for a total of 40 min. The slides were incubated with DISCOVERY Goat Ig Block (760-6008, Ventana) for 32 min at 37 °C followed by application of DISCOVERY Inhibitor (760-4840, Ventana) for 8 min. Afterwards, primary antibodies were dispensed onto the slides (diluted in Discovery Ab diluent, 760-108, Ventana; for specific concentrations and incubation times see Table S2). Primary antibodies were detected using the respective anti-species secondary antibodies conjugated with horseradish peroxidase (HRP; OmniMap anti-rabbit HRP, 760-4311, Ventana; OmniMap anti-mouse HRP, 760-4310, Ventana; OmniMap anti-rat HRP) for 16 min. Next, the corresponding Opal dye (Opal 480 FP150001KT, Opal 520 FP1487001KT, Opal 570 FP1488001KT, Opal 620 FP1495001KT, Opal 690 FP1497001KT, Opal 780 FP1501001KT, Akoya Biosciences) were applied, previously prepared following manufacturer's instructions. After each application of the primary antibody, followed by the corresponding secondary antibody and opal dye (with increasing fluorophore excitation wavelength), an antibody neutralization and denaturation step was applied to remove residual antibodies and HRP, before starting the staining cycle again with the Discovery Inhibitor blocking step. Lastly, samples were counterstained with 4′,6-diamidino-2-phenylindol (DAPI, Roche).

5. FFPE-based mIF imaging. Opal mIF stainings were imaged and digitized using multispectral imaging of the Vectra Polaris (Perkin Elmer) employing the MOTiF technology at X20 magnification for all seven Opal dyes (Opal 480-780) and DAPI. Slides were imaged in a batch manner to ensure identical imaging settings and cross-comparability within each experiment for subsequent image analysis. Unmixing of channels and processing of images were performed with PhenoChart (v.1.0.12) and inForm (v2.4). Images were processed as .qptiff tiles and fused in HALO (Indica Labs, v3.6.4134.396). Pixel resolution 0.5 μm per pixel.

Bidirectional permeability assessment of control compounds

Bidirectional permeability of 4 model compounds on the BIE at 7 days of culture were assessed by washing the chip once with base medium and applying 25 μM atenolol, 1 μM propranolol, 1 μM edoxaban or 1 μM 2-amino-1-methyl-6-phenylimidazo(4,5-*b*) pyridine (PhIP) in culture medium to either the apical or basolateral compartments. The higher concentration of Atenolol was chosen for analytical purposes. To maintain adequate sink conditions, the respective acceptor medium was supplemented with 4% BSA (Sigma Aldrich). The concentration of the compounds in donor and acceptor compartments were analyzed by liquid chromatography–tandem mass spectrometry (LC-MS/MS) after 3 hours of compound exposure at 37 °C, 5% CO_2, 95% humidity. Apparent permeability (P_{app}) was calculated according to eqn (1) and efflux ratios (ER) were calculated using the following formula:

$$ER = \frac{P_{app}(B \rightarrow A)}{P_{app}(A \rightarrow B)} \quad (2)$$

where P_{app} (B → A) is the apparent permeability from the basal to the apical compartment and P_{app} (A → B) is the apparent permeability from the apical to the basal compartment. To assess the specificity of transporter-dependent efflux, P-glycoprotein (P-gp) function was inhibited by addition of 1 μM zosuquidar, while BCRP function was inhibited by addition of 1 μM Ko143. Cascade Blue was added to each compound solution to assess barrier integrity during the assay and BIEs with leaky barriers were excluded from the analysis.

Liquid chromatography-tandem mass spectrometry (LC-MS/MS) analysis

1. Bidirectional permeability experiments. Donor and $C_{don,t=0}$ samples from bidirectional transport studies were diluted in 5-fold volume of culture medium. After, a three-fold volume of acetonitrile containing internal standard was added to all samples. Plates were then centrifuged for 10 min at 6300 rpm and 5 °C. Supernatant was collected and kept at −20 °C until further analysis.

Analysis was performed by using a liquid chromatography-tandem mass spectrometry (LC-MS/MS). In brief, a Shimadzu 30 AD pump (Shimadzu) was connected to a HTS PAL autosampler (CTC Analytics) and a QTRAP 6500 mass spectrometer (Sciex) having an electrospray ionization source. Further details on LC-MS/MS parameters can be found in Tables S3 and S4. All compounds were analyzed in positive ionization mode. Samples' concentration was then determined by taking the peak area ratio between analyte and internal standard. Mass balance of all compounds after three hours of incubation was >85%, calculated according to the following formula:

$$\mathrm{MB\%} = \frac{C_{acc} \times V_{acc} + C_{don} \times V_{don}}{C_{don,t=0} \times V_{don}} \quad (3)$$

where $C_{acc/don}$ denotes concentration in the acceptor or donor compartment, $V_{acc/don}$ the volume in the acceptor or donor compartment and $C_{don,t=0}$ the initial concentration at the start of the experiment.

2. Midazolam study-parent and metabolite quantification. Samples of cell culture media were removed from the apical and basolateral compartments of the OpenTop OrganoChip at the time points detailed in Table S7. Without a cell barrier gravitational flows occur across the hydrogel, caused by repeated sampling and unlevelling of the apical and basolateral compartments. In the earliest apical and basolateral sampling point mass balance of midazolam was observed which indicates negligible non-specific binding to the hydrogel. To ensure functional barrier integrity, tissues were assessed using cascade blue both the day before and immediately after the experimental time-course, as previously described. Tissues exhibiting an apparent permeability value below the 25 nm s^{-1} threshold were excluded from the study. Samples were diluted in deionized ultrapure water 1 : 3 sample : water and immediately stored at −20 °C until a single sample preparation and analysis procedure was performed. As preparation, samples were quenched with a solution of acetonitrile with a 5 ng mL^{-1} labetalol internal standard in the ratio of 3 : 1 quenching solution : sample, centrifuged at 4500 rpm for 60 min at 4 °C, supernatants were collected and analyzed by liquid chromatography tandem mass spectrometry (LC-MS/MS). The instrumental set-up was comprised of a Shimadzu LC30AD/Shimadzu SIL30ACMP/Shimadzu CTO30A UHPLC system, a QTRAP6500 mass spectrometer (Sciex) and a TurboSpray ion source (550 °C). Ion acquisition was completed in positive MRM mode for midazolam, 1′-OH-midazolam, 1′-OH-midazolam and the internal standard. Additional details about the LC-MS/MS analysis such as the analytical columns, mobile phases and retention times are reported in Tables S5 and S6. Calibration curves of midazolam and its two measured metabolites were used for quantitative analysis, with sample dilution corresponding to the linear range of each molecule's calibration curve. For quality control of the analysis, 4 control concentrations were measured in duplicates, with an acceptance criterion of 20% precision and 25% at the limit of quantification.

Measurement of CYP3A4 activity

Comparison of CYP3A4 activity in BIE, TW organoid monolayers and Caco-2 TW monolayers was assessed with the P450-Glo CYP3A4 assay kit with a luciferin-IPA substrate (V9001; Promega, WI, USA). For a positive control, the cultured systems were incubated with the CYP3A4 inducer rifampicin (25 μM) for 48 hours (days 8–10 in organoid-based systems and days 19–21 in Caco-2 TW monolayers). To isolate any effect of the DMSO vehicle (final concentration 0.1%) on CYP3A4 activity, all cultured systems had controls that were exposed to DMSO in parallel to the rifampicin induction. An inhibition control was established in the cultured systems *via* induction for 48 hours with rifampicin, followed by incubation with selective CYP3A4 inhibitor ketoconazole (1 μM) for half an hour prior to addition of the luciferin-IPA substrate for 60 min (37 °C, 5% CO_2). The apical supernatant was collected, the detection agent added and equilibrated at room temperature for 20 min. Luminescence was measured with the Flex station 3 plate at 1000 milliseconds integration. To normalize across the different cell culture systems, cells were lysed with RIPA buffer and the protein was quantified with Pierce's BCA Protein Assay kit following manufacturer instructions.

In silico analysis of midazolam time-concentration data and estimation of intestinal DMPK parameters

The pharmacokinetic analysis of midazolam was conducted using concentration-time profiles obtained from the apical and basolateral compartments of the OpenTop OrganoChip along with the fixed input BIE and intestinal DMPK parameters (Table S7). A compartmental model was employed to represent the apical, cellular, and basolateral compartments. Key pharmacokinetic parameters, intestinal intrinsic clearance ($CL_{int,gut}$) and intestinal permeability (P_{app}), were estimated and $CL_{int,gut}$ subsequently scaled according to the unbound fraction in the medium ($CL_{u,int,gut}$), which was experimentally determined. The compartmental modeling and data fitting were performed using Phoenix NLME (version 3.5.4, Certara, Pennsylvania, USA). The fitting approach utilized was the naive pooled method available in Phoenix, which processes data from multiple replicates by accounting for the associated prediction error of the parameters, without incorporating inter-well variability.

The F_G was calculated using the Q_{gut} model using the eqn (1) and (4)–(6) and compared with the *in vivo* value for midazolam as reported in the literature.[4]

$$CL_{perm} = P_{app} \times A_{int} \quad (4)$$

$$Q_{gut} = \frac{CL_{perm} \times Q_{ent}}{Q_{ent} + CL_{perm}} \quad (5)$$

$$F_G = \frac{Q_{gut}}{Q_{gut} + CL_{u,int,gut}} \quad (6)$$

where CL_{perm} refers to the permeability clearance, A_{int} *in vivo* intestinal surface area estimated as 200 m^2 in previous literature and Q_{ent} an average of enterocytic blood flow previously estimated at 18 L h^{-1}.[54,55]

Conclusions

This work explores pharmaceutical sciences applications of a bioengineered intestinal epithelium with physiologically relevant geometric patterning designed to enhance tissue reproducibility, maturity and barrier function. Key findings from this work include reproducible crypt-axis regional tissue patterning, with barrier function demonstrated through routine permeability assays with similar barrier performance to Caco-2 standards. The presence of key drug transporters (DTs) and drug-metabolizing enzymes (DMEs) was confirmed, although further optimization of organoid media may further enhance their representation. Phenotypic and functional differences in organoid lines highlight the need for further evaluation and objective comparison of organoid lines to their donor tissue to distinguish what is reflective of patient diversity. The platform's utility for performing classical drug transport assays was demonstrated, along with the functional validation of P-gp and BCRP through targeted inhibition studies. Lastly, a proof-of-concept study combined *in vitro*/*in silico* mechanistic modeling approaches. Within a single *in vitro* experiment, three intestinal ADME processes were modelled with data collected in a quantifiable and time-resolved manner. This allows for *in vitro* evaluation of permeability, phase I and II metabolism and active efflux of the metabolites. With additional validation and further correlation to *in vivo* patient data, it could prove a useful tool for predicting absorption behavior of different compound groups and new modalities, not only in healthy patients, but also different disease and age groups that reflect population dynamics. This approach has significant potential to improve oral drug formulation and safety assessment, offering a more comprehensive understanding of drug permeability and metabolism in the human gut.

Author contributions

E. G., S. M. S., N. M., and N. G. conceived the study; E. G., S. M. S. and N. G. wrote the manuscript; M. N. designed and fabricated the fluidic device and crypt stamps with support from J. A.; M. N. generated artwork design; I. P. performed finite element simulations. E. G. and S. M. S. designed and performed most experiments in the manuscript; R. L. S., M. F. H., and M. N. optimized epithelium growth conditions; I. S. and S. M. S. isolated organoid lines from primary tissue; M. M. and M. Z. performed RNAseq; M. B. and T. K.-T. performed the computational analysis of RNAseq data, with support from E. G. and S. M. S for data interpretation. M. F. H. co-developed the histomold; I. C. performed FFPE processing, sectioning, H&E and AlcianBlue/PAS stainings, with support from M. F. H.; M. F. H. performed immunohistochemistry, mIF stainings, imaging and analysis; I. S. performed flow cytometry experiments and analysis; S. S. performed LC-MS/MS analysis; J. K., C. S., M. H., S. F., N. M. and N. G. supported with data interpretation; all authors read and approved the manuscript.

Conflicts of interest

All authors are current employees of Hoffmann-La Roche Ldt or were employed by the company while working on this study. The company provided support in the form of salaries for authors but did not have any additional role in the study design, data collection and analysis, decision to publish or preparation of the manuscript. Hoffmann-La Roche Ldt. has filed for patent protection on the OrganoChip OpenTop described herein. M. N., and N. G. are named as inventors on the patent.

Data availability

Data for this article, including bulk RNA sequencing data, are available on the NCBI SRA repository at **https://www.ncbi.nlm.nih.gov/sra/PRJNA1271604**.

Supplementary information is available. See DOI: **https://doi.org/10.1039/d5lc00626k**.

Acknowledgements

We thank Regine Gerard for help with organoid isolation and establishment; the 360 Labs (Strategy, Portfolio and Operations, Roche Pharma Research and Early Development), specifically Michael Zaayman, for their support with infrastructure and sequencing experiments, as well as Hana Glier for her support in FACS sorting primary tissue material; Anke Gehringer for logistical support; Kristina Kromer for FACS sorting aid; and Matthias P. Lutolf for contribution to the development of the fluidic device holding the bioengineered tissues.

Notes and references

1 M. Stielow, A. Witczyńska, N. Kubryń, Ł. Fijałkowski, J. Nowaczyk and A. Nowaczyk, *Molecules*, 2023, **28**, 8038.
2 T. Nakanishi and I. Tamai, *Curr. Drug Metab.*, 2015, **16**, 753–764.

3 N. Milani, N. Parrott, D. O. Franyuti, P. Godoy, A. Galetin, M. Gertz and S. Fowler, *Lab Chip*, 2022, **22**, 2853–2868.
4 M. Davies, P. Peramuhendige, L. King, M. Golding, A. Kotian, M. Penney, S. Shah and N. Manevski, *Drug Metab. Dispos.*, 2020, **48**, 1169–1182.
5 S. Kourula, M. Derksen, F. Jardi, S. Jonkers, M. van Heerden, P. Verboven, V. Theuns, S. Van Asten, T. Huybrechts, A. Kunze, E. Frazer-Mendelewska, K. W. Lai, R. Overmeer, J. L. Roos, R. G. J. Vries, S. F. Boj, M. Monshouwer, F. Pourfarzad and J. Snoeys, *Eur. J. Pharm. Sci.*, 2023, **188**, 106481.
6 T. Zietek, P. Giesbertz, M. Ewers, F. Reichart, M. Weinmüller, E. Urbauer, D. Haller, I. E. Demir, G. O. Ceyhan, H. Kessler and E. Rath, *Front. Bioeng. Biotechnol.*, 2020, **8**, 577656.
7 K. Tanaka, T. Mochizuki, S. Baba, S. Kawai, K. Nakano, T. Tachibana, K. Uchimura, A. Kato, T. Miyayama, T. Yamaguchi, H. Nishihara, K. Terao and Y. Kato, *Sci. Rep.*, 2025, **15**, 11403.
8 E. J. Streekstra, M. Keuper-Navis, J. J. M. W. van den Heuvel, P. van den Broek, M. W. J. Stommel, S. Bervoets, L. O'Gorman, R. Greupink, F. G. M. Russel, E. van de Steeg and S. N. de Wildt, *Eur. J. Pharm. Sci.*, 2024, **201**, 106877.
9 A. Sharma, L. Jin, X. Wang, Y.-T. Wang and D. M. Stresser, *Lab Chip*, 2024, **24**, 339–355.
10 M. Kasendra, R. Luc, J. Yin, D. V. Manatakis, G. Kulkarni, C. Lucchesi, J. Sliz, A. Apostolou, L. Sunuwar, J. Obrigewitch, K.-J. Jang, G. A. Hamilton, M. Donowitz and K. Karalis, *eLife*, 2020, **9**, e50135.
11 T. Imaoka, R. Onuki-Nagasaki, H. Kimura, K. Tai, M. Ishii, A. Nozue, I. Kaisaki, M. Hoshi, K. Watanabe, K. Maeda, T. Kamizono, T. Yoshioka, T. Fujimoto, T. Satoh, H. Nakamura, O. Ando, H. Kusuhara and Y. Ito, *Sci. Rep.*, 2024, **14**, 29921.
12 K. Michiba, K. Maeda, O. Shimomura, Y. Miyazaki, S. Hashimoto, T. Oda and H. Kusuhara, *Drug Metab. Dispos.*, 2022, **50**, 204–213.
13 Y. Harnik, O. Yakubovsky, R. Hoefflin, R. Novoselsky, K. Bahar Halpern, T. Barkai, Y. Korem Kohanim, A. Egozi, O. Golani, Y. Addadi, M. Kedmi, T. Keidar Haran, Y. Levin, A. Savidor, H. Keren-Shaul, C. Mayer, N. Pencovich, R. Pery, D. S. Shouval, I. Tirosh, I. Nachmany and S. Itzkovitz, *Nature*, 2024, **632**, 1101–1109.
14 J. E. Speer, Y. Wang, J. K. Fallon, P. C. Smith and N. L. Allbritton, *J. Biol. Eng.*, 2019, **13**, 82.
15 J. E. Speer, D. B. Gunasekara, Y. Wang, J. K. Fallon, P. J. Attayek, P. C. Smith, C. E. Sims and N. L. Allbritton, *J. Biol. Eng.*, 2019, **13**, 36.
16 M. Keuper-Navis, M. Walles, B. Poller, A. Myszczyszyn, T. K. van der Made, J. Donkers, H. Eslami Amirabadi, M. J. Wilmer, S. Aan, B. Spee, R. Masereeuw and E. van de Steeg, *Pharmacol. Res.*, 2023, **195**, 106853.
17 S. Fowler, W. L. K. Chen, D. B. Duignan, A. Gupta, N. Hariparsad, J. R. Kenny, W. G. Lai, J. Liras, J. A. Phillips and J. Gan, *Lab Chip*, 2020, **20**, 446–467.
18 N. Milani, N. Parrott, A. Galetin, S. Fowler and M. Gertz, *CPT: Pharmacometrics Syst. Pharmacol.*, 2024, **13**, 524–543.
19 R. K. Zwick, P. Kasparek, B. Palikuqi, S. Viragova, L. Weichselbaum, C. S. McGinnis, K. L. McKinley, A. Rathnayake, D. Vaka, V. Nguyen, C. Trentesaux, E. Reyes, A. R. Gupta, Z. J. Gartner, R. M. Locksley, J. M. Gardner, S. Itzkovitz, D. Boffelli and O. D. Klein, *Nat. Cell Biol.*, 2024, **26**, 250–262.
20 N. Gjorevski, M. Nikolaev, T. E. Brown, O. Mitrofanova, N. Brandenberg, F. W. DelRio, F. M. Yavitt, P. Liberali, K. S. Anseth and M. P. Lutolf, *Science*, 2022, **375**, eaaw9021.
21 R. López-Sandoval, M. F. Harter, Q. Yu, L. Gaspa-Toneu, I. Cubela, K. Kromer, J. Aubert, A. M. Filip, L. Kaltenbach, M. Almato-Bellavista, N. Akkerman, Y. Bollen, S. Munteanu, J. Fidelin, A. Augustin, C. Schori, M. Bickle, M. P. Lutolf, T. Recaldin, J. Beumer, M. Nikolaev, N. Gjorevski and J. G. Camp, *bioRxiv*, 2025, preprint, DOI: **10.1101/2025.05.02.651468**.
22 M. Fujii, M. Matano, K. Toshimitsu, A. Takano, Y. Mikami, S. Nishikori, S. Sugimoto and T. Sato, *Cell Stem Cell*, 2018, **23**, 787–793.e6.
23 F. Pan, L. Han, Y. Zhang, Y. Yu and J. Liu, *Int. J. Food Sci. Nutr.*, 2015, **66**, 680–685.
24 M. Boegh and H. M. Nielsen, *Basic Clin. Pharmacol. Toxicol.*, 2015, **116**, 179–186.
25 R. Kumar, T. Islam and M. Nurunnabi, *J. Control. Release*, 2022, **351**, 504–559.
26 I. Bácskay, P. Arany, P. Fehér, L. Józsa, G. Vasvári, D. Nemes, Á. Pető, D. Kósa, Á. Haimhoffer, Z. Ujhelyi and D. Sinka, *Pharmaceutics*, 2025, **17**, 148.
27 Y. Zhang, Z. Wang, Y. Wang, W. Jin, Z. Zhang, L. Jin, J. Qian and L. Zheng, *PeerJ*, 2024, **12**, e18636.
28 M. Ichikawa, H. Akamine, M. Murata, S. Ito, K. Takayama and H. Mizuguchi, *Sci. Rep.*, 2021, **11**, 11670.
29 S. Stegemann, C. Moreton, S. Svanbäck, K. Box, G. Motte and A. Paudel, *Drug Discovery Today*, 2023, **28**, 103344.
30 A. Agha, W. Waheed, N. Alamoodi, B. Mathew, F. Alnaimat, E. Abu-Nada, A. Abderrahmane and A. Alazzam, *Macromol. Mater. Eng.*, 2022, **307**, 2200053.
31 R. G. Rodrigues, P. G. M. Condelipes, R. R. Rosa, V. Chu and J. P. Conde, *Micromachines*, 2023, **14**, 1837.
32 C. C. Douma and M. T. Bowser, *Anal. Chem.*, 2023, **95**, 18379–18387.
33 B. J. van Meer, H. de Vries, K. S. A. Firth, J. van Weerd, L. G. J. Tertoolen, H. B. J. Karperien, P. Jonkheijm, C. Denning, A. P. IJzerman and C. L. Mummery, *Biochem. Biophys. Res. Commun.*, 2017, **482**, 323–328.
34 W. D. Mason, N. Winer, G. Kochak, I. Cohen and R. Bell, *Clin. Pharmacol. Ther.*, 1979, **25**, 408–415.
35 P. A. Routledge and D. G. Shand, *Clin. Pharmacokinet.*, 1979, **4**, 73–90.
36 D. A. Parasrampuria and K. E. Truitt, *Clin. Pharmacokinet.*, 2016, **55**, 641–655.
37 K. H. Dingley, K. D. Curtis, S. Nowell, J. S. Felton, N. P. Lang and K. W. Turteltaub, *Cancer Epidemiol., Biomarkers Prev.*, 1999, **8**, 507–512.
38 G. W. Caldwell, S. M. Easlick, J. Gunnet, J. A. Masucci and K. Demarest, *J. Mass Spectrom.*, 1998, **33**, 607–614.
39 Y. Guo, Y. Xie and J. Qin, *Biotechnol. J.*, 2024, **19**, e2300390.
40 Y. Mai, L. Dou, Z. Yao, C. M. Madla, F. K. H. Gavins, F. Taherali, H. Yin, M. Orlu, S. Murdan and A. W. Basit, *Mol. Pharmaceutics*, 2021, **18**, 1895–1904.

41 W. Siegmund, K. Ludwig, G. Engel, M. Zschiesche, G. Franke, A. Hoffmann, B. Terhaag and W. Weitschies, *J. Pharm. Sci.*, 2003, **92**, 604–610.
42 K. P. Van Ness, F. Cesar, C. K. Yeung, J. Himmelfarb and E. J. Kelly, *Clin. Transl. Sci.*, 2022, **15**, 9–42.
43 J.-U. Peter, P. Dieudonné and O. Zolk, *Pharmacy*, 2024, **17**, 473.
44 M. Gertz, A. Harrison, J. B. Houston and A. Galetin, *Drug. Metab. Dispos.*, 2010, **38**, 1147–1158.
45 S. Chen, Y. Zhou, Y. Chen and J. Gu, *Bioinformatics*, 2018, **34**, i884–i890.
46 A. Dobin, C. A. Davis, F. Schlesinger, J. Drenkow, C. Zaleski, S. Jha, P. Batut, M. Chaisson and T. R. Gingeras, *Bioinformatics*, 2013, **29**, 15–21.
47 Y. Liao, G. K. Smyth and W. Shi, *Bioinformatics*, 2014, **30**, 923–930.
48 H. Li, B. Handsaker, A. Wysoker, T. Fennell, J. Ruan, N. Homer, G. Marth, G. Abecasis, R. Durbin and 1000 Genome Project Data Processing Subgroup, *Bioinformatics*, 2009, **25**, 2078–2079.
49 L. Wang, S. Wang and W. Li, *Bioinformatics*, 2012, **28**, 2184–2185.
50 P. Ewels, M. Magnusson, S. Lundin and M. Käller, *Bioinformatics*, 2016, **32**, 3047–3048.
51 Y. Zhang, G. Parmigiani and W. E. Johnson, *NAR:Genomics Bioinf.*, 2020, **2**, lqaa078.
52 C. W. Law, Y. Chen, W. Shi and G. K. Smyth, *Genome Biol.*, 2014, **15**, R29.
53 M. F. Harter, E. D'Arcangelo, J. Aubert, B. Lavickova, C. Havnar, B. Stoll, I. Cubela, A. M. Filip, L. Gaspa-Toneu, J. Scherer, E. Karagkiozi, J.-S. Dupre, R. López-Sandoval, R. Hsia, L. M. Norona, G. Brancati, R. Okuda, J. G. Camp, E. R. Shamir, J. L. Garcia-Cordero, I. Pereiro and N. Gjorevski, *bioRxiv*, 2025, preprint, DOI: **10.1101/2025.04.01.646522**.
54 J. Yang, M. Jamei, K. R. Yeo, G. T. Tucker and A. Rostami-Hodjegan, *Curr. Drug Metab.*, 2007, **8**, 676–684.
55 D. N. Granger, P. D. Richardson, P. R. Kvietys and N. A. Mortillaro, *Gastroenterology*, 1980, **78**, 837–863.